THE JOURNAL OF PHYSICAL CHEMISTRY C

Article

Cite This: J. Phys. Chem. C XXXX, XXX, XXX−XXX

pubs.acs.org/JPCC

Elucidation of Tip-Broadening Effect in Tip-Enhanced Raman Spectroscopy (TERS): A Cause of Artifacts or Potential for 3D TERS

Rui Wang[†] and Dmitry Kurouski*[,†,‡]

[†]Department of Biochemistry and Biophysics and [‡]The Institute for Quantum Science and Engineering, Texas A&M University, College Station, Texas 77843, United States

Supporting Information

ABSTRACT: The tip-broadening effect (TBE), which makes the apparent dimensions of the imaged objects larger than they truly are, is one of the major disadvantages of atomic force microscope-related technique, like tip-enhanced Raman spectroscopy (TERS). However, the TBE also provides an opportunity to achieve three-dimensional (3D) TERS if the plasmonically active zones located at the shaft of the used tip. Herein, we found that the side part of the *p*-nitrothiophenol (*p*NTP)-modified Au microplates (AuMPs) can be observed when TBE exists. Moreover, the 3D TERS feature was applied to monitor reduction species of *p*NTP catalyzed by Au microplates (AuMPs). Our results showed that the 3D TERS is capable of distinguishing signals from both the side and top part in a single piece of AuMP, corresponding to Au{100} or Au{110} with low catalytic activity and Au{111} with higher catalytic activity, respectively.

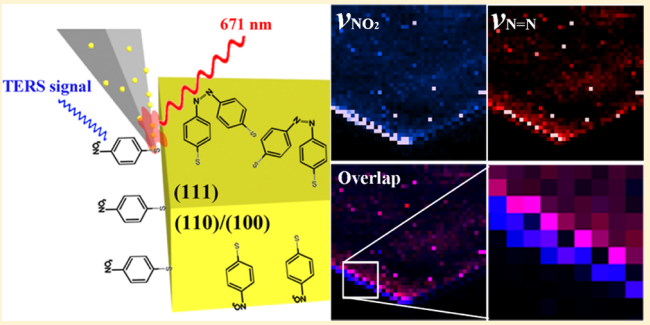

INTRODUCTION

Optical spectroscopy techniques are typically diffraction limited. This limitation can be overcome by a combination with scanning probe microscope, equipped with a metal or metal-coated scanning probe.[1−3] If such a tip is approached on the surface, molecules located directly under it will experience localized electromagnetic field of surface plasmon resonances, coherent oscillations of conduction electrons of metal. This will enable enhancement of Raman scattering from the molecules up to 10^8, which is sufficient for the single molecule detection.[4−6] The metal or metal-coated tip can be rastered above the sample surface with simultaneous collection of enhanced Raman spectra. This will allow for an acquisition of a chemical map of the analyzed specimen with subdiffraction spatial resolution.[7−9]

First developed in 2000,[10−12] this technique, known as tip-enhanced Raman spectroscopy (TERS), became broadly utilized in various research areas ranging from art conservation science to biochemistry and electrochemistry.[13−16] Despite the commercial availability of TER systems, the "Achilles' heel" of this technique is a reproducibility and life time of TER probes. Over the last decade, multiple tip synthetic approaches were developed to overcome this limitation.[17−20] Nevertheless, two synthetic methods are typically used to prepare TER tips: electrochemical etching[21,22] and metal evaporation.[13,23,24] The first method is primarily used for a fabrication of tips for scanning tunneling microscope-based TER systems, whereas metal evaporation is usually employed for tips used in atomic force microscope (AFM)-based TERS. Thermal or electron-beam evaporation produce a thin (20−70 nm) film of a noble metal on commercially available silicon or silicon nitride AFM tips. Their quality may vary batch to batch, but on average these metal-coated tips have a good yield and demonstrate on average 10^4 enhancement.[25−27] From a perspective of the tip geometry, silicon or silicon nitride shaft appears to be covered with thousands of metal nanofeatures that are more prominent for silver-coated[28,29] and less prominent for gold-coated tips.[30] The tip enhancement and its spatial resolution are attributed to a nanofeature formed at the apex of the scanning probe, which comes into direct contact with the sample upon TER measurements.

If the sample is flat, nanofeatures on the tip shaft should play very little if any role in TER imaging. However, in the case of nonflat samples, their contribution can be sufficient due to additionally provided enhancement of shaft nanofeatures (Scheme 1a,b). It is especially concerning for AFM-based platforms, where the tip shaft constantly interacts with sides of imaged objects (Scheme 1c). This makes lateral dimension of imaged objects larger than they are in reality, a phenomenon known as tip-broadening effect (TBE).[31,32]

In this study, we investigated TBE on TER imaging using chemically synthesized Au microplates (AuMPs). These AuMPs have 40−100 nm in height and tens of microns in length. Their top surface has Au{111}, whereas sides have Au{110} or {100} crystal facets. After modification with *p*-nitrothiophenol (*p*NTP) monolayer, both AFM and TER

Received: September 27, 2018
Revised: October 3, 2018
Published: October 10, 2018

DOI: 10.1021/acs.jpcc.8b09455
J. Phys. Chem. C XXXX, XXX, XXX−XXX

Scheme 1. Illustration of TBE of TERS and AFM and Experimental Setup[a]

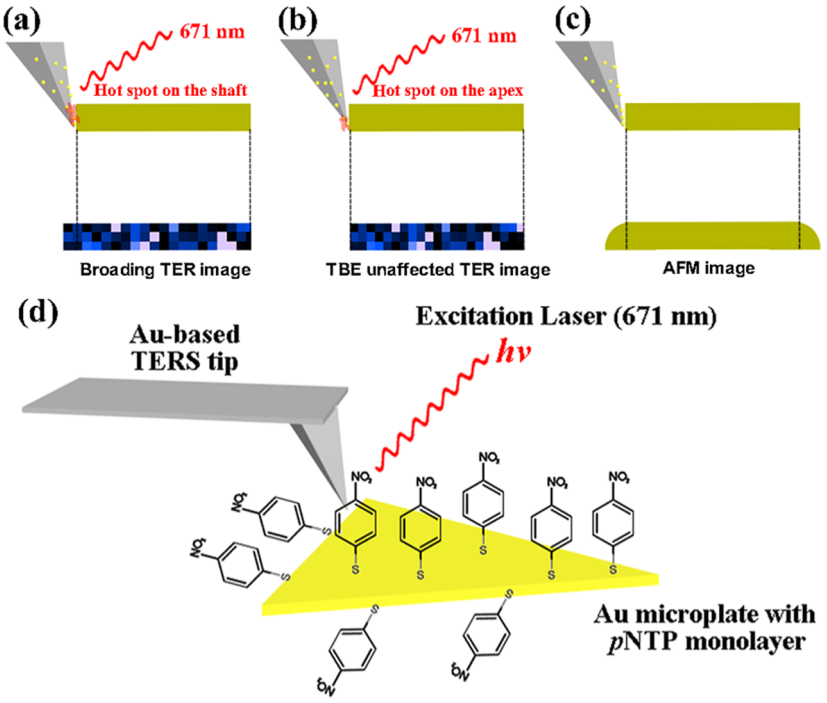

[a]Anticipated contribution of plasmonic nanofeatures at shafts of scanning probes on AFM−TER imaging (a, b) based on TBE of AFM (c). (d) Schematic overview of our experimental setup.

imaging were conducted. Astonishingly, we observed that part of our TER probes would show TBE in TER images, which is similar to the TBE of AFM images (Scheme 1c). Our explanation is that TER imaging may be strongly affected by TBE if used probes have active zones (i.e., hot-spot) at their shafts (Scheme 1a). On the contrary, those TBE-unaffected probes can give higher resolution than AFM due to their highly localized hot-spot on the apex (Scheme 1b). Meanwhile, chemical mapping of the reduced *p*NTP was also conducted by our TER probes. TBE-affected TER images gave clear evidence showing that the top surface ({111}) is more catalytic active than the side part ({110} or {100}) of the AuMPs.

METHODS

Chemicals. Gold(III) chloride trihydrate ($HAuCl_4{\cdot}3H_2O$, 99.9%), hexadecyltrimethylammonium bromide (CTAB, 99%), poly(vinylpyrrolidone) (PVP, average M_w 40 000), diethylene glycol (DEG, 99%), *p*-nitrothiophenol (*p*NTP, 80%), sodium borohydride ($NaBH_4$, 99%) were purchased from Sigma-Aldrich (St. Louis, MO). Ethanol was purchased from Decon Labs (King of Prussia, PA). All chemicals were used as received without purification.

Synthesis of the AuMPs. A typical synthesis of the AuMPs was performed as following. PVP (512 mg) and CTAB (112 mg) were added in 7.2 mL of DEG, and the solution was heated and maintained in a sealed flask at 150 °C to dissolve the surfactants. Then, 0.8 mL of DEG solution containing 9.6 mg of $HAuCl_4{\cdot}3H_2O$ was injected to this solution and it was maintained at 150 °C for 5 min. After that the reaction temperature was increased to 200 °C and maintained for 45 min. Color of the solution changed from yellow, colorless to light brown and finally changed to golden color. Subsequently, the solution was cooled down to room temperature and the AuMPs were precipitated, centrifuged (8000 rpm, 3 min), and washed twice with ethanol. The obtained AuMPs were finally dispersed in 10 mL of ethanol for further use.

***p*NTP Modification of the AuMPs.** The as-synthesized AuMPs were first deposited on precleaned Si wafer. After that the AuMP-deposited Si wafer was immersed in a 5 mM ethanolic *p*NTP solution for 12 h to replace the original ligands, i.e., PVP and CTAB, forming monolayer of *p*NTP on AuMPs. Sonication in ethanol for 5 min was performed to remove any uncoordinated *p*NTP molecule.

AuMP-Catalyzed Reduction of *p*NTP. The *p*NTP-AuMP-deposited Si wafer was immersed in 5 mL of 30 mM aqueous $NaBH_4$ solution for 30 min, followed by rinsing with water and drying.

TER Probe Fabrication. Si AFM tips were purchased from Appnano (Mountain View, CA). The tip force constant, resonance frequency, and amplitude are 2.7 N/m, 50−80 kHz, 20 nm, respectively. The scanning rates for low- and high-magnification TERS image are 125 and 20 nm/s, respectively. For a metal deposition, AFM tips were placed in a thermal evaporator (MBrown, Stratham, NH). Metal deposition was conducted at $\sim 10^{-6}$ mbar by thermal evaporation of gold (Kurt J. Lesker, Efferson Hills, PA) at 0.3 A/s rate to reach 70 nm Au thickness on the AFM tips. Temperature at the tip surface was ~50 °C upon metal deposition.

AFM−TER Imaging. AFM and TER imagings were done on AIST-NT-HORIBA system equipped by 671 nm continuous wave laser. Laser light was brought to the sample in a side-illumination geometry using 100× Mitutoyo microscope objective. Scattered electromagnetic radiation was collected using the same objective and directed to a fiber-coupled HORIBA iHR550 spectrograph equipped with a Synapse EM-CCD camera (HORIBA, Edison, NJ). The signal intensities of the nitro and azo group in all of our TERS images

DOI: 10.1021/acs.jpcc.8b09455
J. Phys. Chem. C XXXX, XXX, XXX−XXX

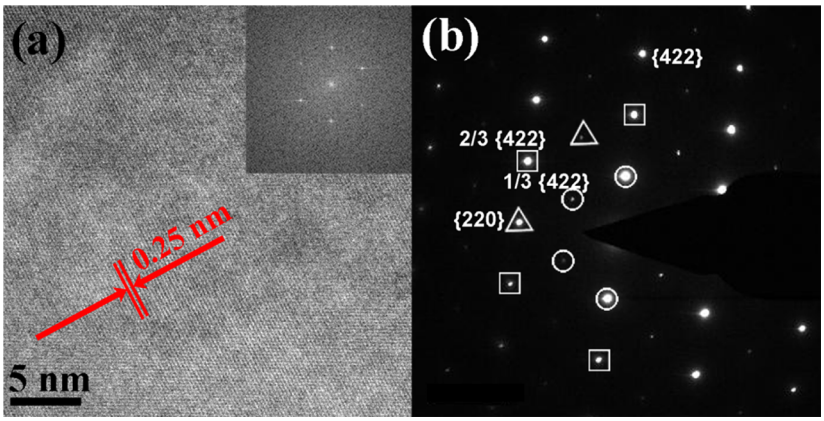

Figure 1. Structural characterization of as-prepared AuMPs. HRTEM image (a), the corresponding fast Fourier transform pattern (inset) and the SAED pattern (b) of the resultant AuMPs. The {220}, 1/3 {422}, and 2/3 {422} reflections are marked with triangle, circle, and rectangle, respectively.

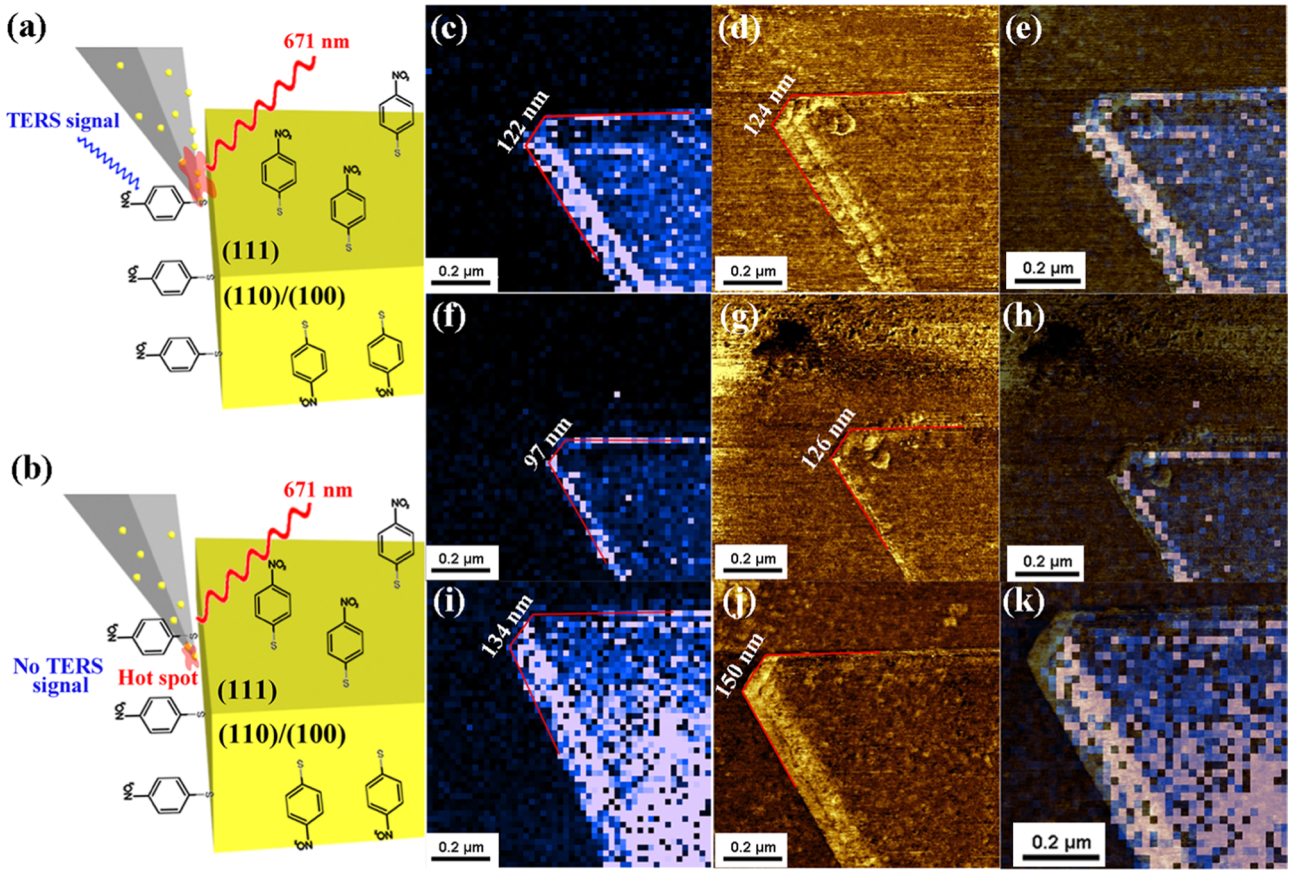

Figure 2. Probe-dependent TBE in TER and AFM images. (a, b) Proposed schemes showing the hot-spot located at both the shaft and apex (a) and only at the apex (b) of the TER probe. (c–e), (f–h), and (i–k) are the TER images (c, f, i), Phase-mode AFM images (d, g, j) and their overlapped images (e, h, k) of TER probes 1, 2, and 3, respectively.

are integrated intensities of 1300–1370 and 1380–1490 cm^{-1}, respectively.

Electron Microscopy. Transmission electron microscopy (TEM), high-resolution transmission electron microscopy (HRTEM), and selected area electron diffraction (SAED) observations were performed with a FEI Tecnai G2 F20 ST field-emission electron microscope with an accelerating voltage of 200 kV. Scanning electron microscopy (SEM) images were obtained on a JEOL JSM-7500F field-emission scanning electron microscope operating at 5 kV.

RESULTS

The AuMPs were prepared by a polyol-based "wet-chemical" process.[33,34] As shown in Figure S1, the as-synthesized AuMPs were generally trigonal and hexagonal plates with 20–50 μm in diameter and 40–100 nm in thickness. HRTEM image and SAED pattern (Figures 1 and S2) demonstrated that these AuMPs were well-grown single crystals with {111} planes as the basal surface. Besides regular Bragg diffractions spots of {220} and {422} facets, the SEAD pattern (Figure 1b) was dominated by kinematically forbidden 1/3 {422} and 2/3

DOI: 10.1021/acs.jpcc.8b09455
J. Phys. Chem. C XXXX, XXX, XXX–XXX

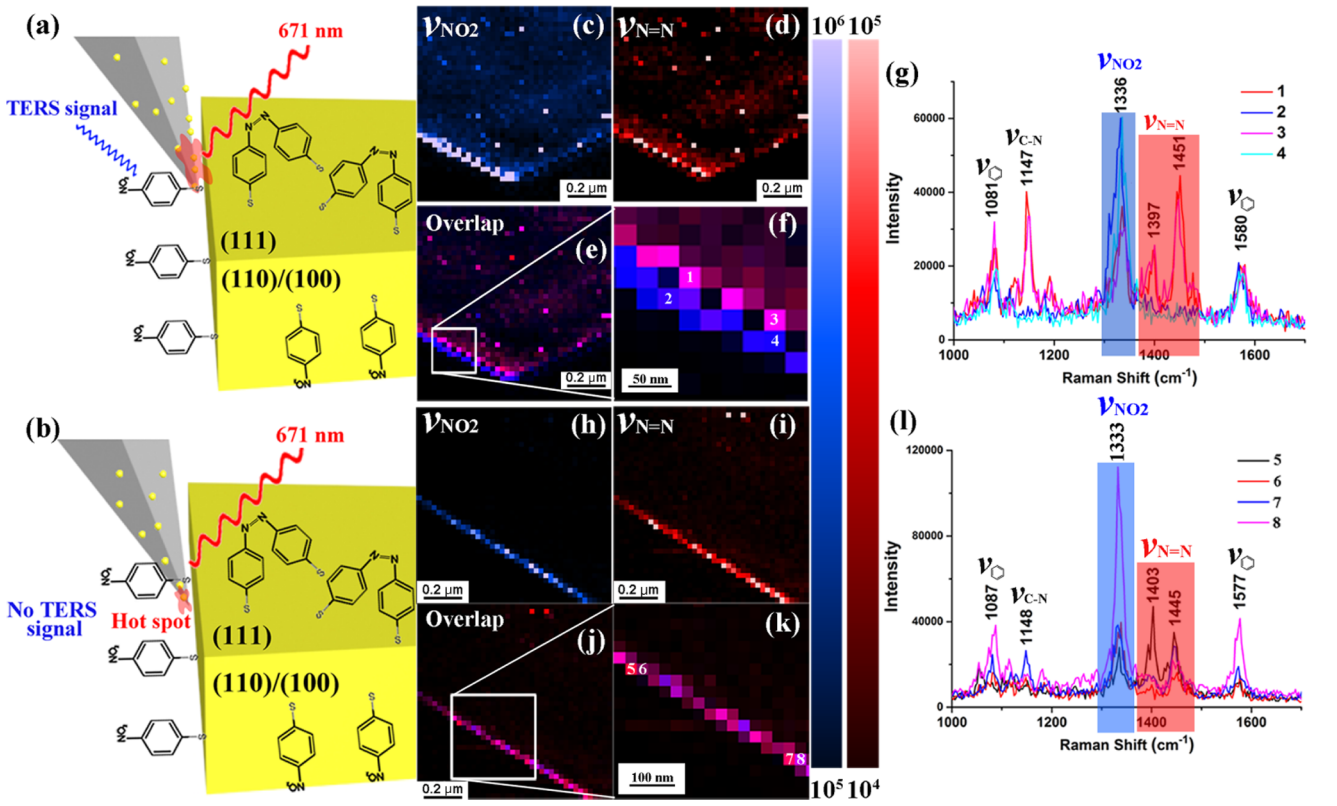

Figure 3. TERS monitoring the facet-dependent reduction of *p*NTP catalyzed by AuMPs. (a, b) Proposed schemes showing the hot-spot located at both the shaft and apex (a) and only at the apex (b) of the TER probe. (c, d), (h, i) HR TER images of the distribution of $-NO_2$ (c, h) and N═N group (d, i) obtained by TER probes 4 and 5, respectively. (e, j) Corresponding overlap images. (f, k) Zoomed-in TER images of the white rectangle position in (e) and (j), respectively. (g, l) Typical TERS spectra extracted from the marked position in (f) and (k).

{422} spots, indicating presence of multiple parallel twin planes on {111} facets parallel to the basal surface of the AuMPs. Moreover, the *d*-space of the lattice planes measured from the HRTEM image (Figure 1a) is ca. 0.25 nm, which is very close to the 3 times of the {422} lattice (or 3 × {422} superlattice) spacing (0.249 nm), also confirmed twin-planes structure with {111} as basal facet. These results are in good agreement to previous reports[35,36] that PVP, a surfactant also used in our synthesis, can be selectively absorbed on the crystal plane of {111} and reduce the growth rate along ⟨111⟩ direction, but enhance those of {110} and {100} planes. Thus, top and bottom facets of the AuMPs are made of {111} facets, whereas the {110} or {100} constructs the side facets. Next, a self-assembled monolayer of *p*NTP was formed on the resulting AuMPs through ligand exchange[37] between *p*NTP and original ligands, i.e., PVP and CTAB.

TER and AFM imagings were performed on AIST-NT-HORIBA TER system using Au-coated probes (Scheme 1d). The images were taken by a side-illumination configuration of with scanning size of 5 × 5 and 1 × 1 μm, and the corresponding resolutions of TER images are 125 nm (low resolution, abbreviated as LR) and 20 nm (high resolution, abbreviated as HR) per pixel. Upon TER probe approaching to the surface of *p*NTP-modified AuMP, strong TER signal was obtained when 671 nm excitation (~20 μW, 1 s integration time) was introduced. As shown in Figure S3, the Raman band at ca. 1336 cm^{-1} can be assigned to the symmetric nitro stretching vibration, whereas the peaks at ca. 1084, 1118, and 1573 cm^{-1} were due to phenyl ring modes.[8]

AFM and TER mappings were conducted by three probes (labeled as TER probe 1, 2, and 3) on a selected corner of single piece of AuMP. From the height-mode AFM images (Figure S4), one could find that obtained dimensions (~125, 150, and 200 nm for TER probes 1, 2, and 3, respectively) of the same AuMP corner vary a lot among these three TER probes. This phenomenon is well known as TBE in the AFM field, which hinders the AFM measuring in lateral dimension, because it is a convolution of the lateral size of the sample and the probe's radius of curvature (Scheme 1c).

Next, we compared the dimensions of the selected corner measured by the HR TER images and phase-mode AFM images. Phase-mode AFM was used here instead of height mode because of its higher spatial resolution. We found that the dimensions of AuMP measured by TER probe 1 are very close: 122 nm for the HR TER vs 124 nm for phase-mode AFM (Figure 2c–e), whereas those measured in HR TER using TER probes 2 and 3 are 29 (Figure 2f–h) and 16 nm (Figure 2i–k) smaller than their AFM counterparts, respectively. This finding indicates the TER probes 2 and 3 are less influenced by TBE than probe 1, i.e., probe-dependent TBE. Meanwhile, the SEM images (Figure S5) showed that TER probe 1 has a broader apex than those of probes 2 and 3. And its shaft surface was dominated by bunches of small nanoparticles, which was not obvious for probes 2 and 3. These unique geometries of probe 1 may play an important role in the TER mapping and are the root of probe-dependent TBE effect. Moreover, two more TER probes were tested on other AuMPs and showed similar results (Figure S6).

DOI: 10.1021/acs.jpcc.8b09455
J. Phys. Chem. C XXXX, XXX, XXX–XXX

These results also suggest that the TER maps can be strongly affected by TBE if used probes have active zones (i.e., hot-spot) at their shafts (Scheme 1a). In contrast, those TBE-unaffected probes can give higher resolution than AFM due to their highly localized hot-spot on their apex (Scheme 1b). In the case of TER probe 1, the hot-spot is located at both the apex and shaft. As can be seen in Figure 2a, the hot-spot at the shaft of the tip interacts intensively with the *p*NTP molecules on the side facets of the AuMPs, leading to a larger lateral dimension of imaged objects than they are, which is the origin of the TBE of TER imaging; In contrast, the hot-spots of TER probes 2 and 3 are mainly located at their apex (Figure 2b), making them avoid the TBE and show higher lateral resolution.

To further verify our hypothesis, the AuMP-catalyzed reduction of *p*NTP to the corresponding aniline derivative by $NaBH_4$ was examined by our TERS technique. It is commonly known that the *p*NTP will be reduced to 4,4′-dimercapto-azobenzene (4,4′-DMAB) or *p*-aminothiophenol and can be easily detected by changes in the Raman bands.[38,39] New vibrational Raman bands at ca. 1147, 1397, and 1451 cm^{-1} were observed upon $NaBH_4$ reduction, which can be assigned to C−N symmetric stretching and N═N stretching modes. Then, TER mapping was conducted based on the original nitro stretching vibration mode (1336 cm^{-1}, labeled as blue) and the new N═N stretching modes (1397 and 1451 cm^{-1}, labeled as red). Figures 3, S7 and S8 showed the TER images of a selected corner of single piece of AuMP imaged by two TER probes (TER probes 4 and 5). Figures S7 and S8 showed that LR TER images obtained based on nitro and N═N matched very well for both of these two TER probes, indicating an evenly catalyzed reduction of our AuMP, which was confirmed by the representative Raman spectrum in Figures S7d and S8d. However, the HR TER images provided more information. For TER probe 4, the outline of the AuMP based on $-NO_2$ group was 1−2 pixels (20−40 nm) larger than that of N═N bond based. Signals of the outmost edges were even dominated by $-NO_2$ group (Figures 3c−g and S9). However, HR TER images obtained by TER probe 5 demonstrated perfect spatial overlap of $-NO_2$ group and N═N bond signal intensities (Figures 3h−l and S10). Meanwhile, AFM images were taken alongside with the TER images (Figures S11 and S12). Figure S11 clearly showed the $-NO_2$ signals obtained by TER probe 4 matched well with the outline of the AFM edge, whereas those obtained by TER probe 5 were 10−20 nm away from the edge (Figure S12). These findings can be well explained by above-mentioned TBE. Similar to TBE-affected TER images showed in Figure 2c−e, the dimension of TER image (based on $-NO_2$ group) obtained by TER probe 4 was very close to their AFM counterpart, indicating that it was also affected by TBE. In other words, the outmost of the $-NO_2$ signals was actually coming from the side part of the AuMP, which is {110} or {100} facet. Correspondingly, TER image obtained by TER probe 5 was not affected by TBE, as it showed higher resolution than AFM image. It is important to highlight that the positions where these HR TER and AFM images were taken from were very close (several micrometers away) on the same piece of AuMP, further proving that the TBE is probe-dependent and related to the hot-spot locations. Another interesting finding on these HR TER images is the signal intensities at the edge of the AuMP were much stronger than those at the interior counterparts (not always like this, see Figures S13−S15). Moreover, six more TER probes were tested on different areas (TER probes 6−11, Figures S13−S18). Half of these probes could give these broadening $-NO_2$ TER images (Figures S13, S15, and S16). Therefore, these HR TER images strongly indicate that these signal differences are probe-dependent and related to the above-mentioned TBE.

DISCUSSION

The catalytic property of noble metal nanomaterials (including Au, Ag, Pd, etc.) is strongly dependent on the exposed surfaces, like {111}, {110}, and {100}, found in our AuMPs. From a catalysis application point of view, the noble-metal nanomaterials exposed by different crystal facets will behave very differently in terms of catalytic performance.[40−42] However, little attention has been paid to the facet-dependent catalytic property of gold nanomaterials due to the lack of characterization methods.[43−45] The TBE-affected TER images of AuMPs show that TERS can provide a solution. As shown in Figure S19, the signals of edge of AuMPs, which were constructed by low catalytic active {110} and {100} facets, were dominated by $-NO_2$ group, whereas the reduction mostly took place at the basal part of AuMPs, corresponding to the {111} facet with higher catalytic activity. It should be pointed out that the catalysis contribution of the twin-planed structure[46] of AuMPs is still unknown so far. Moreover, different from the TERS work have done before, one can speculate about three-dimensional chemical mapping arising from our TBE of AFM−TERS systems.

CONCLUSIONS

Our results showed that TBE should be seriously considered upon AFM−TER imaging of nonflat objects. We demonstrated that plasmonically active zones of the tip shaft could contribute to the collected TER signals. Accurate elimination or deconvolution of TER signals from such additional enhancement is a very complicated process, especially if the imaged object is heterogeneous or has a sophisticated chemical structure. We believe that several research groups noticed this TBE upon TER imaging or TERS characterization of their samples, but were not able to elucidate what exactly causing observed TER spectral variability. For instance, Sereda and Lednev[47] reported that TER spectra collected from the top surface of polypeptide microcrystal were very consistent and similar to the far-field spectrum of this crystal. However, TER spectra that were collected from the edge of the crystal have randomly appearing vibrational bands and were drastically different than the spectra collected from the top of the microcrystal. Our results suggest that the observed spectral heterogeneities in those experiments were due to TBE of the used tips, which were also fabricated by metal thermal evaporation. Unfortunately, it is nearly impossible to predict the presence and location of hot-spots on TER tips since such information cannot be extracted from any existing techniques. Moreover, SEM examination of tips prior to TER imaging is not feasible since such SEMed tips typically have no plasmonic activity. Our reported results are very timely, since the TERS field is slowly transitioning from single-spectral acquisition from the surface of the object of interest to TER imaging.

DOI: 10.1021/acs.jpcc.8b09455
J. Phys. Chem. C XXXX, XXX, XXX−XXX

■ ASSOCIATED CONTENT

Supporting Information

The Supporting Information is available free of charge on the ACS Publications website at DOI: 10.1021/acs.jpcc.8b09455.

TEM image of AuMPs; representative TER spectrum; height-mode AFM images; SEM images of probes 1, 2, and 3; LR TER images obtained by probes 4 and 5; additional TER images obtained by other probes; proposed reduction mechanism of *p*NTP-modified AuMPs (PDF)

■ AUTHOR INFORMATION

Corresponding Author

*E-mail: dkurouski@tamu.edu.

ORCID

Dmitry Kurouski: 0000-0002-6040-4213

Notes

The authors declare no competing financial interest.

■ ACKNOWLEDGMENTS

We are grateful to AgriLife Research of Texas A&M for the provided financial support. We also acknowledge Governor's University Research Initiative (GURI) grant program of Texas A&M University, GURI Grant Agreement No. 12-2016. Use of the TAMU Materials Characterization Facility is acknowledged. Use of the TAMU Microscopy and Imaging Center and Dr Hansoo Kim are acknowledged. The authors thank Charles Farber for valuable discussions.

■ REFERENCES

(1) Hartschuh, A. Tip-enhanced near-field optical microscopy. *Angew. Chem., Int. Ed.* **2008**, *47*, 8178−8191.

(2) Wang, X.; Huang, S. C.; Huang, T. X.; Su, H. S.; Zhong, J. H.; Zeng, Z. C.; Li, M. H.; Ren, B. Tip-enhanced Raman spectroscopy for surfaces and interfaces. *Chem. Soc. Rev.* **2017**, *46*, 4020−4041.

(3) Schultz, Z. D.; Marr, J. M.; Wang, H. Tip enhanced Raman scattering: plasmonic enhancements for nanoscale chemical analysis. *Nanophotonics* **2014**, *3*, 91−104.

(4) Zhang, R.; Zhang, Y.; Dong, Z. C.; Jiang, S.; Zhang, C.; Chen, L. G.; Zhang, L.; Liao, Y.; Aizpurua, J.; Luo, Y.; et al. Chemical mapping of a single molecule by plasmon-enhanced Raman scattering. *Nature* **2013**, *498*, 82−86.

(5) Jiang, N.; Foley, E. T.; Klingsporn, J. M.; Sonntag, M. D.; Valley, N. A.; Dieringer, J. A.; Seideman, T.; Schatz, G. C.; Hersam, M. C.; Van Duyne, R. P. Observation of multiple vibrational modes in ultrahigh vacuum tip-enhanced Raman spectroscopy combined with molecular-resolution scanning tunneling microscopy. *Nano Lett.* **2012**, *12*, 5061−5067.

(6) Sonntag, M. D.; Klingsporn, J. M.; Garibay, L. K.; Roberts, J. M.; Dieringer, J. A.; Seideman, T.; Scheidt, K. A.; Jensen, L.; Schatz, G. C.; Van Duyne, R. P. Single-Molecule Tip-Enhanced Raman Spectroscopy. *J. Phys. Chem. C* **2012**, *116*, 478−483.

(7) Rahaman, M.; Rodriguez, R. D.; Plechinger, G.; Moras, S.; Schüller, C.; Korn, T.; Zahn, D. R. T. Highly Localized Strain in a MoS2/Au Heterostructure Revealed by Tip-Enhanced Raman Spectroscopy. *Nano Lett.* **2017**, 6027−6033.

(8) van Schrojenstein Lantman, E. M.; Deckert-Gaudig, T.; Mank, A. J.; Deckert, V.; Weckhuysen, B. M. Catalytic processes monitored at the nanoscale with tip-enhanced Raman spectroscopy. *Nat. Nanotechnol.* **2012**, *7*, 583−586.

(9) Zhong, J. H.; Jin, X.; Meng, L.; Wang, X.; Su, H. S.; Yang, Z. L.; Williams, C. T.; Ren, B. Probing the electronic and catalytic properties of a bimetallic surface with 3 nm resolution. *Nat. Nanotechnol.* **2017**, *12*, 132−136.

(10) Anderson, M. S. Locally enhanced Raman spectroscopy with an atomic force microscope. *Appl. Phys. Lett.* **2000**, *76*, 3130−3132.

(11) Stöckle, R. M.; Suh, Y. D.; Deckert, V.; Zenobi, R. Nanoscale chemical analysis by tip enhanced Raman spectroscopy. *Chem. Phys. Lett.* **2000**, *318*, 131−136.

(12) Hayazawa, N.; Inouye, Y.; Sekkat, Z.; Kawata, S. Metallized tip amplification of near-field Raman scattering. *Opt. Commun.* **2000**, *183*, 333−336.

(13) Kurouski, D.; Mattei, M.; Van Duyne, R. P. Probing Redox Reactions at the Nanoscale with Electrochemical Tip-Enhanced Raman Spectroscopy. *Nano Lett.* **2015**, *15*, 7956−7962.

(14) Kurouski, D.; Zaleski, S.; Casadio, F.; Van Duyne, R. P.; Shah, N. C. Tip-enhanced Raman spectroscopy (TERS) for in situ identification of indigo and iron gall ink on paper. *J. Am. Chem. Soc.* **2014**, *136*, 8677−8684.

(15) Martín Sabanés, N.; Ohto, T.; Andrienko, D.; Nagata, Y.; Domke, K. F. Electrochemical TERS Elucidates Potential-Induced Molecular Reorientation of Adenine/Au (111). *Angew. Chem., Int. Ed.* **2017**, *56*, 9796−9801.

(16) Jiang, N.; Chiang, N.; Madison, L. R.; Pozzi, E. A.; Wasielewski, M. R.; Seideman, T.; Ratner, M. A.; Hersam, M. C.; Schatz, G. C.; Van Duyne, R. P. Nanoscale chemical imaging of a dynamic molecular phase boundary with ultrahigh vacuum tip-enhanced Raman spectroscopy. *Nano Lett.* **2016**, *16*, 3898−3904.

(17) Huang, T. X.; Huang, S. C.; Li, M. H.; Zeng, Z. C.; Wang, X.; Ren, B. Tip-enhanced Raman spectroscopy: tip-related issues. *Anal. Bioanal. Chem.* **2015**, *407*, 8177−8195.

(18) Ren, B.; Picardi, G.; Pettinger, B.; Schuster, R.; Ertl, G. Tip-enhanced Raman spectroscopy of benzenethiol adsorbed on Au and Pt single-crystal surfaces. *Angew. Chem., Int. Ed.* **2005**, *44*, 139−142.

(19) Opilik, L.; Dogan, Ü.; Szczerbiński, J.; Zenobi, R. Degradation of silver near-field optical probes and its electrochemical reversal. *Appl. Phys. Lett.* **2015**, *107*, No. 091109.

(20) Schmid, T.; Yeo, B. S.; Leong, G.; Stadler, J.; Zenobi, R. Performing tip-enhanced Raman spectroscopy in liquids. *J. Raman Spectrosc.* **2009**, *40*, 1392−1399.

(21) Stadler, J.; Schmid, T.; Zenobi, R. Nanoscale chemical imaging using top-illumination tip-enhanced Raman spectroscopy. *Nano Lett.* **2010**, *10*, 4514−4520.

(22) Zeng, Z. C.; Huang, S. C.; Wu, D. Y.; Meng, L. Y.; Li, M. H.; Huang, T. X.; Zhong, J. H.; Wang, X.; Yang, Z. L.; Ren, B. Electrochemical Tip-Enhanced Raman Spectroscopy. *J. Am. Chem. Soc.* **2015**, *137*, 11928−11931.

(23) Agapov, R. L.; Sokolov, A. P.; Foster, M. D. Protecting TERS probes from degradation: extending mechanical and chemical stability. *J. Raman Spectrosc.* **2013**, *44*, 710−716.

(24) Kurouski, D.; Deckert-Gaudig, T.; Deckert, V.; Lednev, I. K. Structure and composition of insulin fibril surfaces probed by TERS. *J. Am. Chem. Soc.* **2012**, *134*, 13323−13329.

(25) Kurouski, D.; Deckert-Gaudig, T.; Deckert, V.; Lednev, I. K. Surface characterization of insulin protofilaments and fibril polymorphs using tip-enhanced Raman spectroscopy (TERS). *Biophys. J.* **2014**, *106*, 263−271.

(26) He, Z.; Voronine, D. V.; Sinyukov, A. M.; Liege, Z. N.; Birmingham, B.; Sokolov, A. V.; Zhang, Z.; Scully, M. O. Tip-Enhanced Raman Scattering on Bulk MoS 2 Substrate. *IEEE J. Sel. Top. Quantum Electron.* **2017**, *23*, 113−118.

(27) Deckert-Gaudig, T.; Taguchi, A.; Kawata, S.; Deckert, V. Tip-enhanced Raman spectroscopy−from early developments to recent advances. *Chem. Soc. Rev.* **2017**, *46*, 4077−4110.

(28) Hayazawa, N.; Yano, T.-a.; Kawata, S. Highly reproducible tip-enhanced Raman scattering using an oxidized and metallized silicon cantilever tip as a tool for everyone. *J. Raman Spectrosc.* **2012**, *43*, 1177−1182.

(29) Asghari-Khiavi, M.; Wood, B. R.; Hojati-Talemi, P.; Downes, A.; McNaughton, D.; Mechler, A. Exploring the origin of tip-enhanced Raman scattering; preparation of efficient TERS probes with high yield. *J. Raman Spectrosc.* **2012**, *43*, 173−180.

(30) Pashaee, F.; Tabatabaei, M.; Caetano, F. A.; Ferguson, S. S.; Lagugne-Labarthet, F. Tip-enhanced Raman spectroscopy: plasmid-free vs. plasmid-embedded DNA. *Analyst* **2016**, *141*, 3251−3258.
(31) Canet-Ferrer, J.; Coronado, E.; Forment-Aliaga, A.; Pinilla-Cienfuegos, E. Correction of the tip convolution effects in the imaging of nanostructures studied through scanning force microscopy. *Nanotechnology* **2014**, *25*, No. 395703.
(32) Shen, J.; Zhang, D.; Zhang, F.-H.; Gan, Y. AFM tip-sample convolution effects for cylinder protrusions. *Appl. Surf. Sci.* **2017**, *422*, 482−491.
(33) Liu, H.; Yang, Q. A two-step temperature-raising process to gold nanoplates with optical and surface enhanced Raman spectrum properties. *CrystEngComm* **2011**, *13*, 2281−2288.
(34) Kan, C.; Wang, G.; Zhu, X.; Li, C.; Cao, B. Structure and thermal stability of gold nanoplates. *Appl. Phys. Lett.* **2006**, *88*, No. 071904.
(35) Kan, C.; Wang, C.; Li, H.; Qi, J.; Zhu, J.; Li, Z.; Shi, D. Gold microplates with well-defined shapes. *Small* **2010**, *6*, 1768−1775.
(36) Kan, C.; Zhu, X.; Wang, G. Single-Crystalline Gold Microplates: Synthesis, Characterization, and Thermal Stability. *J. Phys. Chem. B* **2006**, *110*, 4651−4656.
(37) Yu, C.; Varghese, Leo; Irudayaraj, J. Surface Modification of Cetyltrimethylammonium Bromide-Capped Gold Nanorods to Make Molecular Probes. *Langmuir* **2007**, *23*, 9114−9119.
(38) Xie, W.; Herrmann, C.; Kompe, K.; Haase, M.; Schlucker, S. Synthesis of bifunctional Au/Pt/Au Core/shell nanoraspberries for in situ SERS monitoring of platinum-catalyzed reactions. *J. Am. Chem. Soc.* **2011**, *133*, 19302−19305.
(39) Chen, J.; Zhang, R.; Han, L.; Tu, B.; Zhao, D. One-pot synthesis of thermally stable gold@mesoporous silica core-shell nanospheres with catalytic activity. *Nano Res.* **2013**, *6*, 871−879.
(40) Fujita, T.; Guan, P.; McKenna, K.; Lang, X.; Hirata, A.; Zhang, L.; Tokunaga, T.; Arai, S.; Yamamoto, Y.; Tanaka, N.; Erlebacher, J.; Chen, M.; et al. Atomic origins of the high catalytic activity of nanoporous gold. *Nat. Mater.* **2012**, *11*, 775−780.
(41) Zhou, K.; Li, Y. Catalysis based on nanocrystals with well-defined facets. *Angew. Chem., Int. Ed.* **2012**, *51*, 602−613.
(42) Zhang, L.; Niu, W.; Xu, G. Synthesis and applications of noble metal nanocrystals with high-energy facets. *Nano Today* **2012**, *7*, 586−605.
(43) Li, Y.; Liu, Q.; Shen, W. Morphology-dependent nanocatalysis: metal particles. *Dalton Trans.* **2011**, *40*, 5811−5826.
(44) Nigra, M. M.; Ha, J.-M.; Katz, A. Identification of site requirements for reduction of 4-nitrophenol using gold nanoparticle catalysts. *Catal. Sci. Technol.* **2013**, *3*, 2976−2983.
(45) Wunder, S.; Lu, Y.; Albrecht, M.; Ballauff, M. Catalytic Activity of Faceted Gold Nanoparticles Studied by a Model Reaction: Evidence for Substrate-Induced Surface Restructuring. *ACS Catal.* **2011**, *1*, 908−916.
(46) Kirkland, A. I.; Jefferson, D. A.; Duff, D. G.; Edwards, P. P.; Gameson, I.; Johnson, B. F. G.; Smith, D. J. Structural studies of trigonal lamellar particles of gold and silver. *Proc. R. Soc. A* **1993**, *440*, 589−609.
(47) Sereda, V.; Lednev, I. K. Two Mechanisms of Tip Enhancement of Raman Scattering by Protein Aggregates. *Appl. Spectrosc.* **2017**, *71*, 118−128.

DOI: 10.1021/acs.jpcc.8b09455
J. Phys. Chem. C XXXX, XXX, XXX−XXX